SCIENCE CHINA Materials ARTICLES

mater.scichina.com link.springer.com

Published online 22 March 2019 | https://doi.org/10.1007/s40843-019-9412-5
Sci China Mater 2019, 62(8): 1151–1161

Synthesis, characterization, and theoretical analysis of three new nonlinear optical materials $K_7MRE_2B_{15}O_{30}$ (M= Ca and Ba, RE= La and Bi)

Zhiqing Xie[1†], Ying Wang[1†], Shichao Cheng[1], Guopeng Han[1,2], Zhihua Yang[1] and Shilie Pan[1*]

ABSTRACT **Three new complex borate compounds $K_7CaBi_2B_{15}O_{30}$, $K_7CaLa_2B_{15}O_{30}$ and $K_7BaBi_2B_{15}O_{30}$ have been synthesized by the high-temperature solution method. $K_7CaLa_2B_{15}O_{30}$ and $K_7CaBi_2B_{15}O_{30}$ crystallize in the chiral trigonal space group *R*32, while $K_7BaBi_2B_{15}O_{30}$ crystallizes in the noncentrosymmetric orthorhombic polar space group $Pca2_1$. All of the title compounds have similar three-dimensional crystal structures, which are composed of isolated B_5O_{10} groups and LaO_6 or BiO_6 octahedra, and K^+, Ca^{2+}, and Ba^{2+} cations fill into the cavities to keep charge balance. Based on our research, in the system of $K_7M^{II}RE_2B_{15}O_{30}$ (M^{II} = Ca, Sr, Ba, Zn, Cd, Pb, K/$RE_{0.5}$; RE = Sc, Y, La, Gd, Lu, Bi), $K_7BaBi_2B_{15}O_{30}$ is unique and crystallizes in a different space group, which enriches the structural chemistry of borate. Detailed structural analyses indicate that the structural variation is due to the difference in size and coordination number of the alkaline-earth metal cations. Besides, UV-Vis-NIR spectroscopy analysis and the second-harmonic generation (SHG) measurement on the powder samples show that $K_7CaBi_2B_{15}O_{30}$ exhibits a UV cutoff edge (about 282 nm) and a moderate SHG response (about 0.6 × KDP). In addition, thermal analysis and infrared spectroscopy were also presented. To better understand the structure-property relationships of the title compounds, the first-principles calculations have been performed.**

Keywords: borate, nonlinear optical materials, SHG response, structure-properties relationship

INTRODUCTION

Nonlinear optical (NLO) materials have drawn considerable attention to date for their wide applications, such as material processing, information communication, and photochemical synthesis [1–7]. Numbers of famous NLO crystals have been obtained, including β-BaB_2O_4 (β-BBO) [8], LiB_3O_5 (LBO) [9], CsB_3O_5 (CBO) [10], $CsLiB_6O_{10}$ (CLBO) [11], $KBe_2BO_3F_2$ (KBBF) [12], $Sr_2Be_2B_2O_7$ [13], $K_2Al_2B_2O_7$ (KAB) [14], $KTiOPO_4$ (KTP) [15], KH_2PO_4 (KDP) [16], $AgGaQ_2$ (Q = S, Se) [17,18], and $ZnGeP_2$ (ZGP) [19], which can expand the spectral ranges of solid state lasers from deep-ultraviolet (DUV) to infrared (IR). In the UV and DUV range, borates play a dominant role for their various structural features [20–24], wide transparency window, and large second-harmonic generation (SHG) response [25–30]. For example, β-BBO exhibits large SHG response about 6× KDP and its UV cutoff edge is at about 189 nm; LBO and KBBF not only possess large SHG response about 3× and 1.2× KDP, but also show short UV cutoff edge at about 160 and 155 nm, respectively. The excellent properties of alkali and alkaline metal borates inspirit us to explore new NLO materials in borate systems.

In general, large SHG response is necessary for a potential NLO material. It is well known that SHG response can be enhanced by introducing anions with π-conjugated molecular orbitals (BO_3^{2-}, NO_3^{3-}, CO_3^{2-}, etc.) [26,31–38], the cations with a stereoactive lone pair (Pb^{2+}, Bi^{3+}, etc.) [5,39–43], d^0 transition-metal cations with second-order Jahn-Teller distortion (Ti^{4+}, Nb^{5+}, etc.) [15,44], or polar displacement of d^{10} cation center (Zn^{2+}, Cd^{2+}, etc.) [45,46]. In addition, some previous work [29,47–52] reported that rare-earth (RE) cations (Sc^{3+}, Y^{3+}, La^{3+}, Gd^{3+}, etc.) with deformed REO_n polyhedra are the important sources to enhance the SHG response. For

[1] CAS Key Laboratory of Functional Materials and Devices for Special Environments, Xinjiang Technical Institute of Physics & Chemistry, CAS; Xinjiang Key Laboratory of Electronic Information Materials and Devices, Urumqi 830011, China
[2] Center of Materials Science and Optoelectronics Engineering, University of Chinese Academy of Sciences, Beijing 100049, China
[†] These two authors contributed equally to this work.
[*] Corresponding author (email: slpan@ms.xjb.ac.cn)

example, La-O, Y-O, and Gd-O polyhedra make large contributions to the overall SHG coefficients in $La_2CaB_{10}O_{19}$, $La_9Na_3B_8O_{27}$, $REAl_3(BO_3)_4$ (RE = Y, Gd) and $RECa_4O(BO_3)_3$ (RE = Y, Gd).

Given the above ideas, three new noncentrosymmetric borates $K_7CaBi_2B_{15}O_{30}$ (**I**), $K_7CaLa_2B_{15}O_{30}$ (**II**), and $K_7BaBi_2B_{15}O_{30}$ (**III**) were synthesized. Here, the syntheses, structures, thermal behavior, IR spectrum, UV-Vis-NIR spectrum, and NLO properties of the title compounds are presented. To better understand the structure-properties relationship, the theoretical calculation based on the density functional theory (DFT) was applied for electronic structure analyses.

EXPERIMENTAL SECTION

Reagents

KF (Shanghai Aladdin Reagent Co., Ltd., 99.9%), K_2CO_3 (Tianjin HongYan Chemical Reagent Co., Ltd., 99.0%), $CaCO_3$ (Tianjin YaoHua Chemical Reagent Co., Ltd., 99.0%), $BaCO_3$ (Tianjin HongYan Chemical Reagent Co., Ltd., 99.0%), Bi_2O_3 (Tianjin Bodi Chemical Co., Ltd., 99.0%), La_2O_3 (Shanghai Aladdin Reagent Co., Ltd., 99.0%), B_2O_3 (Shanghai Aladdin Reagent Co., Ltd., 99.9%) and H_3BO_3 (Tianjin HongYan Chemical Co., Ltd., 99.5%) were used as received.

Single-crystal growth

Crystalline samples of the title compounds were obtained by spontaneous crystallization method. The solutions were prepared in platinum crucibles by melting a mixture of $Bi_2O_3/CaCO_3/KF/H_3BO_3$ for Compound **I**, $La_2O_3/CaCO_3/KF/H_3BO_3$ for Compound **II**, $Bi_2O_3/BaCO_3/KF/H_3BO_3$ for Compound **III**, with the molar ratio of 1:1:15:29, 1:1:16:30, 1:1:18:31, respectively. Firstly, the platinum crucibles were placed in the constant temperature zone of a vertical programmable temperature furnace. They were held at 300°C for 10 h to decompose H_3BO_3. Next, the crucibles were heated to 870/850/870°C for Compounds **I**, **II**, and **III** at the rate of 10°C min^{-1} and held at these temperatures for 10 h until the solution became transparent and clear. And then the crucibles were cooled down to 600°C at the rate of 1°C h^{-1}, and finally cooled to ambient temperature at a rate of 15°C h^{-1}. The colorless and transparent crystals of the title compounds were obtained. However, the yields of Compounds **II** and **III** were very low.

Single-crystal X-ray diffraction (XRD)

The crystal structures data of the title compounds were collected by single-crystal XRD on a Bruker SMART APEX II 4K CCD diffractometer using monochromatic Mo Kα radiation with λ = 0.71073 Å at 296(2) K and integrated with the SAINT program [53]. All calculations were performed with programs from the SHELXTL and Olex2 crystallographic program package [54–56]. These structures were checked for possible higher symmetry using the ADDSYM algorithm from the program PLATON [57]. Table 1 lists the crystal data, details of data collections and structure refinement information. Tables S1–S3 in the Supplementary information summarize the equivalent isotropic displacement parameters and atomic coordinates. In order to obtain reasonable *R* value for Compound **III**, the K^+ and Ba^{2+} ions are treated as a mixed occupancy model. As shown in Table S3, the K^+ and Ba^{2+} ions are disordered over four sites, with a set occupancy of 94%/6% (K(5)/Ba(4)), 65%/35% (K(6)/Ba(1)), 51%/49% (K(7)/Ba(2)), 92%/8% (K(8)/Ba(3)) on each site, whereas K^+ and Ca^{2+} are not disordered in Compounds **I** and **II**. Tables S4–S6 present the selected bond distances.

Synthesis and powder X-ray diffraction

Polycrystalline samples of the title compounds were synthesized *via* a solid-state reaction. The raw materials $Bi_2O_3/CaCO_3/K_2CO_3/B_2O_3$, $La_2O_3/CaCO_3/K_2CO_3/B_2O_3$, $Bi_2O_3/BaCO_3/K_2CO_3/B_2O_3$ in the molar ratio of 1:1:3.5:7.5, 1:1:3.5–5:7.5, 1:1:3.5–5:7.5 for Compounds **I**, **II** and **III** were ground thoroughly, packed tightly in a platinum crucible, and heated to 700–750°C at a rate of 20°C h^{-1} with several intermediate grindings. Compound **I** was held at 700°C for 72 h with several intermediate grindings, and the pure polycrystalline samples were obtained, which was confirmed by powder XRD (PXRD) measurements (Fig. 4b). However, pure polycrystalline samples of Compounds **II** and **III** failed to be synthesized, and the major phases of the powder samples were listed in Table S7, and shown in Figs S1 and S2.

Thermal behavior analysis

Thermal gravimetric (TG) analysis and differential scanning calorimetry (DSC) of Compound **I** were carried out on a simultaneous NETZSCH STA 449C thermal analyzer instrument in Pt crucibles with a heating rate of 5°C min^{-1}. The measurement range extended from 35 to 1,000°C in a nitrogen atmosphere.

Infrared spectroscopy

Infrared (IR) spectroscopy was conducted in order to specify the coordination of boron in Compound **I**. IR

Table 1 Crystal data and structures refinement for $K_7CaBi_2B_{15}O_{30}$, $K_7CaLa_2B_{15}O_{30}$ and $K_7BaBi_2B_{15}O_{30}$

Empirical formula	$K_7CaBi_2B_{15}O_{30}$	$K_7CaLa_2B_{15}O_{30}$	$K_7BaBi_2B_{15}O_{30}$
Formula weight	1,373.89	1,233.75	1,470.9
Temperature (K)	296(2)	296(2)	296.15
Crystal system, space group	Trigonal, *R*32	Trigonal, *R*32	Orthorhombic, $Pca2_1$
Unit cell dimensions (Å)	a = 13.3316(16) b = 13.3316(16) c = 14.989(4)	a = 13.453(4) b = 13.453(4) c = 15.239(9)	a = 18.369(2) b = 9.2238(11) c = 18.386(2)
Volume (Å^3)	2307.1(7)	2388.6(18)	3115.3(6)
Z	3	3	4
Absorption coefficient (mm^{-1})	12.654	3.832	13.566
F(000)	1,902	1,746	2,680
Completeness	99.80%	99.70%	99.80%
GOF on F^2	1.122	1.093	1.016
Final R indices [$F_o^2 > 2\sigma(F_o^2)$][a]	R_1 = 0.0340, wR_2 = 0.0797	R_1 = 0.0520, wR_2 = 0.1292	R_1 = 0.0362, wR_2 = 0.0767
R indices (all data)[a]	R_1 = 0.0390, wR_2 = 0.0826	R_1 = 0.0560, wR_2 = 0.1337	R_1 = 0.0434, wR_2 = 0.0796
Absolute structure parameter	0.054(17)	0.09(7)	0.042(9)

a) $R_1 = \Sigma||F_o|-|F_c||/\Sigma|F_o|$ and $wR_2 = [\Sigma w(F_o^2-F_c^2)^2/\Sigma wF_o^4]^{1/2}$ for $F_o^2 > 2\sigma(F_o^2)$.

spectrum was recorded on a Shimadzu IR Affinity-1 FT-IR spectrometer in the range of 4,000–400 cm^{-1}.

UV-Vis-NIR diffuse reflectance spectrum

The UV-Vis-NIR diffuse-reflectance spectrum of Compound **I** was obtained on a Shimadzu SolidSpec-3700DUV spectrophotometer at room temperature. Data were collected in the wavelength range from 190 to 2,600 nm.

NLO measurements

The NLO measurements were performed on the powder samples of Compound **I** by the Kurtz-Perry method [58]. The polycrystalline samples were pressed into a 0.2-mm thick quartz cell and irradiated by a Q-switched Nd:YVO_4 solid-state laser (1,064 nm, 10 kHz, 10 ns). The polycrystalline samples of Compound **I** were ground and sieved into distinct particle size ranges, 20–38, 38–55, 55–88, 88–105, 105–150, and 150–200 μm, and the crystalline KDP samples with the same sizes served as the references.

Numerical calculation details

Electronic structure calculations were given to further understand and interpret the electrical and optical properties of the title compounds. In all these calculations, the CASTEP module based on the total plane-wave pseudopotential method of Materials Studio package has been employed [59–61]. The total energy was calculated with DFT using Perdew-Burke-Ernzerhof (PBE) with generalized gradient approximation (GGA) function [62,63]. Under the norm-conserving pseudopotential (NCP), the following orbital electrons were treated as valence electrons: K: $3s^23p^64s^1$; Ca: $3p^64s^2$; La: $4p^65d^16s^2$; Bi: $4f^{14}5d^{10}6s^26p^3$; B: $2s^22p^1$, and O: $2s^22p^4$. The numbers of plane waves included in the basis sets were determined by a cutoff energy of 880.0 eV, and the Monkhorst-Pack scheme k-points grid sampling was set at 3 × 3 × 3 for the Brillouin zone for Compounds **I** and **II**. The other parameters and convergent criteria were the default values of CASTEP code.

The SHG conversion efficiency of an NLO crystal is significantly determined by the magnitudes of the SHG coefficients when realizing the phase matching. And the SHG coefficient components are relevant to the second-order nonlinear susceptibilities, $d = \chi/2$. By using the band structure results from the CASTEP package [61,64], the second-order nonlinear susceptibilities at the limit of zero frequency, $\chi_{\alpha\beta\gamma}^{(2)}(0)$, can be expressed as the sum of the contribution of the virtual-electron (VE) processes and the virtual-hole (VH) processes [65,66]:

$$\chi_{\alpha\beta\gamma}^{(2)} = \chi_{\alpha\beta\gamma}^{(2)}(\mathrm{VE}) + \chi_{\alpha\beta\gamma}^{(2)}(\mathrm{VH}), \tag{1}$$

$$\chi_{\alpha\beta\gamma}^{(2)}(\mathrm{VE}) = \frac{e^3}{2\hbar^2 m^3}\sum_{vcc'}\int\frac{d^3k}{4\pi^3}P(\alpha\beta\gamma) \times \mathrm{Im}\left[P_{vc}^{\alpha}P_{cc'}^{\beta}P_{c'v}^{\gamma}\right]\left(\frac{1}{\omega_{cv}^3\omega_{vc'}^2}+\frac{1}{\omega_{vc}^4\omega_{c'v}}\right), \tag{2}$$

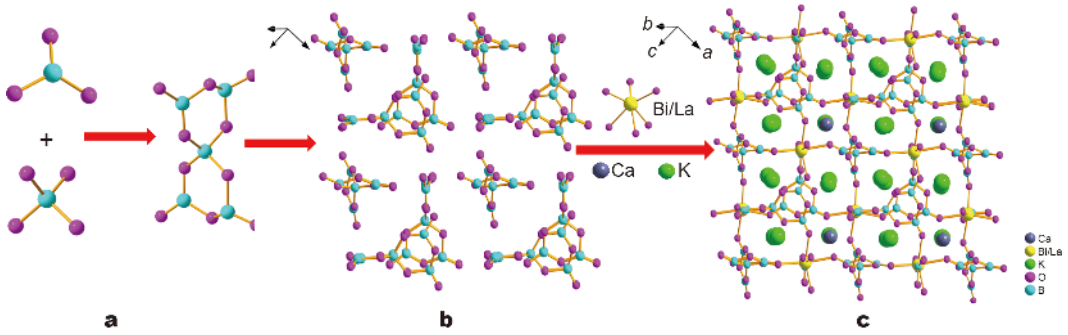

Figure 1 (a) The BO_3, BO_4, and B_5O_{10} groups. (b) The arrangement of B–O groups in $K_7CaBi_2B_{15}O_{30}$ and $K_7CaLa_2B_{15}O_{30}$. (c) The whole 3D crystal structures of $K_7CaBi_2B_{15}O_{30}$ and $K_7CaLa_2B_{15}O_{30}$.

$$\chi^{(2)}_{\alpha\beta\gamma}(\mathrm{VH}) = \frac{e^3}{2\hbar^2 m^3}\sum_{vv'c}\int\frac{d^3k}{4\pi^3}P(\alpha\beta\gamma) \times \mathrm{Im}\left[P^{\alpha}_{vv'}P^{\beta}_{cv'}P^{\gamma}_{vc}\right]\left(\frac{1}{\omega^3_{cv}\omega^2_{vc}}+\frac{1}{\omega^4_{vc}\omega_{cv'}}\right). \quad (3)$$

Here, α, β and γ are the Cartesian components, and v/v', c/c' denote valence bands (VBs) and conduction bands (CBs). And $P(\alpha\beta\gamma)$, $\hbar\omega_{ij}$ and P^{α}_{ij} refer to full permutation, the band energy difference and the momentum matrix elements, respectively.

RESULTS AND DISCUSSION

Crystal structures of $K_7CaBi_2B_{15}O_{30}$ and $K_7CaLa_2B_{15}O_{30}$

$K_7CaBi_2B_{15}O_{30}$ (**I**) and $K_7CaLa_2B_{15}O_{30}$ (**II**) are isostructural and crystallize in the chiral trigonal crystal system group *R*32 (No. 155). In the asymmetric units of Compounds **I** and **II**, there are three unique K atoms, one unique Ca atom, one unique La or Bi atom, three unique B atoms and five unique O atoms, respectively (Tables S1, S2). In the structures of Compounds **I** and **II**, all kinds of B atoms connect with three or four O atoms to form BO_3 triangles or BO_4 tetrahedra, and they link together to form the B_5O_{10} groups *via* sharing vertex O atoms (Fig. 1a). And all of the B_5O_{10} groups are arranged in an isolated configuration without connecting with other B or B-containing units (Fig. 1b). The La and Bi atoms are bonded to six O atoms to form LaO_6 or BiO_6 octahedra. Then the B_5O_{10} groups share four vertical O atoms with neighboring LaO_6 or BiO_6 octahedra to form a three-dimension (3D) framework. The K^+ and Ca^{2+} cations are located in the cavities to keep charge balance (Fig. 1c).

For Compounds **I** and **II**, the K atoms connect with six or eight O atoms to form KO_6 or KO_8 polyhedra with K–O bond lengths ranging from 2.731(7)–3.083(8) Å and 2.775(8)–3.234(10) Å, respectively. The Ca atoms of Compounds **I** and **II** are coordinated to six O atoms to form octahedra with Ca–O bond lengths 2.344 and 2.370 Å, respectively. And the bond lengths of La–O and Bi–O are in the range of 2.291(7)–2.380(6) Å and 2.337(7)–2.435(9) Å, respectively. For Compound **I**, the triangularly coordinated B atoms have B–O distances in the range of 1.307(13)–1.401(14) Å and the tetrahedral B atoms exhibit longer B–O distances in the range of 1.454(11)–1.473(11) Å. For Compound **II**, the triangularly coordinated B atoms have B–O distances in the range of 1.272(16)–1.437(13) Å and the tetrahedral B atoms have longer B–O distances in the range of 1.437(13)–1.491(12) Å.

Crystal structure of $K_7BaBi_2B_{15}O_{30}$

$K_7BaBi_2B_{15}O_{30}$ (**III**) crystallizes in the orthorhombic polar space group $Pca2_1$ (No. 29). Within the asymmetric unit, there are four unique K atoms, four unique K/Ba atoms, two unique Bi atoms, fifteen B atoms and thirty O atoms (Table S3). In the structure, similar to Compounds **I** and **II**, Compound **III** exhibits a complex 3D structure. All of the fifteen B atoms form twelve BO_3 triangles and three BO_4 tetrahedra, and each BO_4 tetrahedra connect with four BO_3 triangles to form three types of B_5O_{10} groups (Fig. 2a). Furthermore, each B_5O_{10} group connects with four distorted BiO_6 octahedra *via* its vertex O atoms (Fig. 2b), and the alternate connection between them gives rise to a 3D framework. And all of K^+ and K^+/Ba^{2+} cations locate in the cavities to keep charge balance (Fig. 2c).

For Compound **III**, the K atoms bond to six or eight O atoms to form KO_6 or KO_8 polyhedra with the K–O bond lengths in the range of 2.693(13)–3.142(3) Å. Each K/Ba atom coordinates to six or eight O atoms to form K/BaO_6 and K/BaO_8 polyhedra, with K/Ba–O bond lengths ranging from 2.663(10) to 3.142(13) Å. The bond lengths of Bi–O are in the range of 2.246(11)–2.487(11) Å. The triangularly coordinated B atoms have B–O distances in

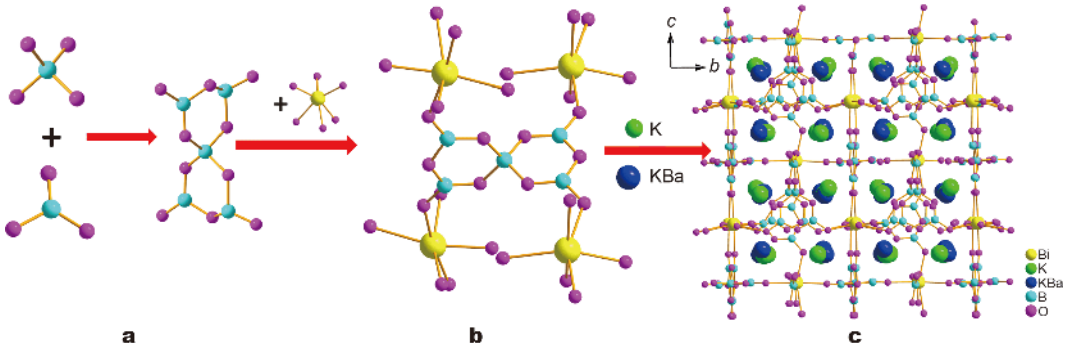

Figure 2 (a) The BO_3, BO_4, and B_5O_{10} groups. (b) The connection of B_5O_{10} groups and BiO_6 polyhedra. (c) The whole 3D crystal structure of $K_7BaBi_2B_{15}O_{30}$.

the range of 1.310(2)–1.440(2) Å and the tetrahedral B atoms have longer B–O distances in the range of 1.437(18)–1.511(19) Å. The bond valence sums of all atoms in the title compounds are in a reasonable range according to the bond valence theory [67].

Effect of cation size on the framework structures

All of the title compounds $K_7MRE_2B_{15}O_{30}$ (M= Ca and Ba, RE= La, and Bi) are stoichiometrically equivalent, and share a common structural style, that is, a 3D network is formed by the B_5O_{10} groups and the REO_6 octahedra. The alkali and alkaline earth metal cations occupy the respective cavities formed by the B_5O_{10} groups and the REO_6 octahedra. However, Compounds **I** and **II** are isostructural in the space group *R*32, which is different from Compound **III** (*Pca*2_1). The size of the alkaline earth metal cations should be responsible for this different framework. Compared with the Bi^{3+} (ion radius = 108) cations, the La^{3+} (ion radius =106.1) cations have the similar ionic radius, and contribute little to the different framework structures. Consequently, Compounds **I** and **II** are isostructural. Compared with smaller Ca^{2+} (ion radius = 99) cations, the requirement of the K^+/Ba^{2+} (ion radius =133/135) cations for a six-fold or eight-fold coordination environment leads to the relatively incompact connection of the 3D network formed by the BiO_6 octahedra and the B_5O_{10} groups. The spaces occupied by the Ca^{2+} cations of Compounds **I** and **II** are not large enough for K^+/Ba^{2+} to reside in Compound **III**. When larger K^+/Ba^{2+} cations are introduced into the crystal structures of Compounds **I** and **II**, a structural strain is produced in the framework. To minimize this strain, the framework needs to be destroyed, which decreases the symmetry from *R*32 space group to *Pca*2_1 space group. The arrangement of Ca–O–B in Compounds **I** and **II**, and K/Ba–O–B groups in Compound **III** are shown in Fig. S3. Although K/BaO_n (n = 6, 8) and CaO_6 polyhedra all connect with the B–O groups in these compounds, the configurations and arrangement are different. Especially, Fig. 3a and b show the configurations of Ca^{2+} and $K(6)^+/Ba(1)^{2+}$ cations, which have a similar configurated environment. In Compounds **I** and **II**, the Ca–O–B angles are 131.792° and in the range of 132.012°–132.056°, the Ca–O–La and Ca–O–Bi angles are 93.971° and range from 92.58° to 92.606°, respectively (Table S10). However, in Compound **III**, the $K(6)^+/Ba(1)^{2+}$–O–B and $K(6)^+/Ba(1)^{2+}$–O–Bi angles are in the ranges of 105.668°–122.458° and 92.547°–96.477° (Table S10), respectively. Obviously, Compounds **I** and **II** show a similar arrangement for B–O groups. On the other hand, there exist large angles changes for the B–O groups and the Bi–O polyhedra in Compound **III** after introducing K(6)/Ba(1) atoms compared with Compounds **I** and **II** as shown in Fig. 3c and d. Moreover, the distortion for RE–O polyhedra in the title compounds was calculated. The results show that the BiO_6 (0.949) octahedra in Compound **III** has larger distortion values for BiO_6 (0.281) and LaO_6 (0.277) octahedra than those in Compounds **I** and **II** (Table S9), which can be attributed to the introduction of K/Ba atoms. Consequently, the difference in size for the alkaline-earth metal cations is the major factor, which leads to the different framework structures of the title compounds.

Thermal analysis

The TG and DSC curves and XRD patterns of Compound **I** are shown in Fig. 4. The DSC curves indicate that there is only one endothermic peak at 725°C on the heating curve. And no obvious weight loss is observed from 30 to 1,000°C according to the TG curve. To further verify the thermal characteristics, polycrystalline powders were put into a platinum crucible and heated to 800°C, and then slowly cooled to room temperature. The PXRD pattern of

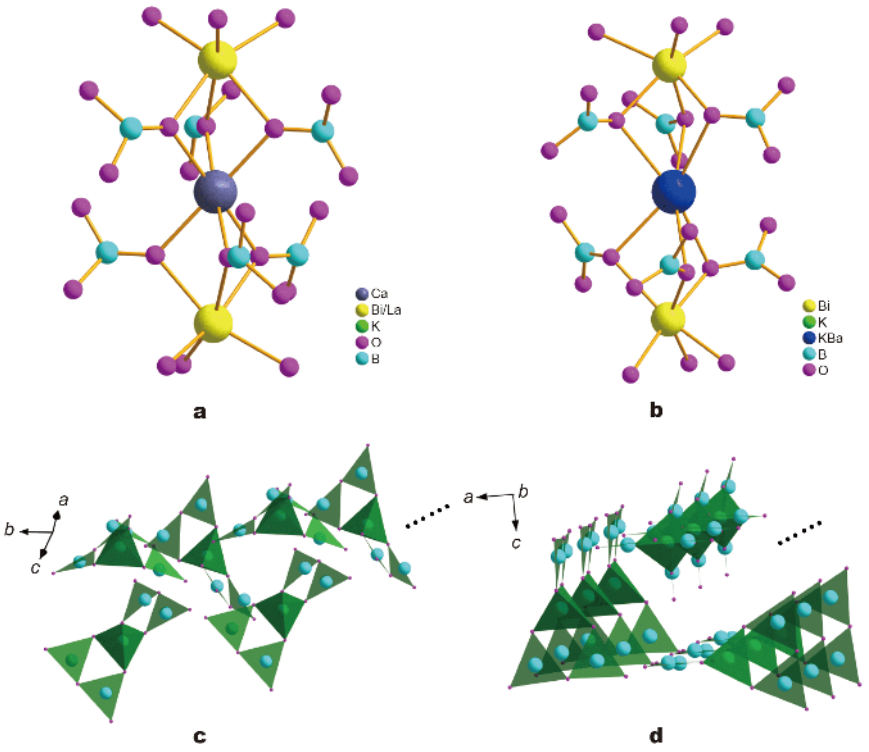

Figure 3 (a) The configuration of Ca^{2+} cation in $K_7CaBi/La_2B_{15}O_{30}$. (b) The configuration of K^+/Ba^{2+} cation in $K_7BaBi_2B_{15}O_{30}B_5O_{10}$ groups. (c) The repeating arrangement of B_5O_{10} groups in $K_7CaBi_2B_{15}O_{30}$ and $K_7CaLa_2B_{15}O_{30}$. (d) The repeating arrangement of B_5O_{10} groups in $K_7BaBi_2B_{15}O_{30}$.

Compound **I** after melting is different from that of Compound **I** before-melting (Fig. 4b). The results suggest that Compound **I** melts incongruently. For the incongruent melting compounds, large single crystals should be grown from the high temperature solution by using the flux method.

Optical properties

IR and UV-Vis-NIR diffuse reflectance spectra

To confirm the coordination surroundings of Compound **I**, IR spectrum was carried out and the results are shown in Fig. S4. According to the previous literatures [47,48,68–70], the characteristic peaks of Compound **I** can be described as follows: the peaks at 1,338, 1,262, and 1,194 cm^{-1} are mainly due to the asymmetric stretching of the BO_3 units, and the peak at 1,020 cm^{-1} is attributed to the BO_4 asymmetric stretching vibration. The peak at 931 cm^{-1} can be assigned to the symmetric stretching of BO_3. The peaks at 766 and 724 cm^{-1} can be assigned to the symmetric stretching of BO_4 while the peak located at 609 cm^{-1} likely comes from the bending vibrations of BO_3 and BO_4 groups. IR spectrum confirms the existence of BO_3 and BO_4 units in Compound **I**. The UV-Vis-NIR diffuse reflectance spectrum reveals that Compound **I** has a short UV cutoff edge at about 282 nm and owns a moderate optical band gap of 3.8 eV, which indicates that Compound **I** has a wide transparency range from UV to NIR range (Fig. 5).

NLO measurements

Based on the noncentrosymmetric crystal structure of Compound **I**, it should possess NLO properties. The curves of SHG intensities as a function of particle size are shown in Fig. 6. The SHG intensities increase with the increasing particle sizes before they become constant, which is consistent with phase-matching behavior. When the particle size is about 150–200 μm, Compound **I** exhibits an SHG efficiency of about 0.6 times that of KDP. According to the anionic group theory [71] of NLO activity in borates, the B–O groups can make a large contribution. Especially, the BO_3 trigonal planes make more contribution to the SHG effects than the BO_4 tetrahedra. In addition, the BiO_6 octahedra, as NLO-active units, also have nonnegligible contributions according to previous studies [39,41,42]. Consequently, the magnitudes of di-

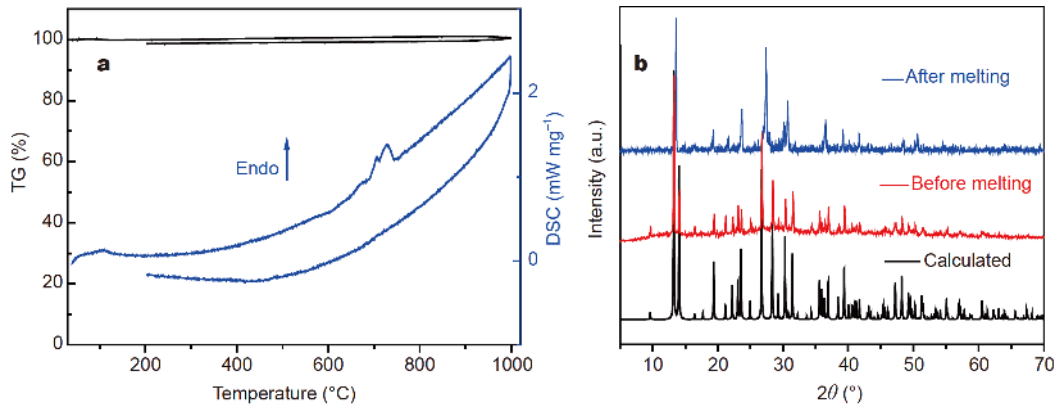

Figure 4 The TG-DSC curves (a) and XRD patterns (b) of $K_7CaBi_2B_{15}O_{30}$.

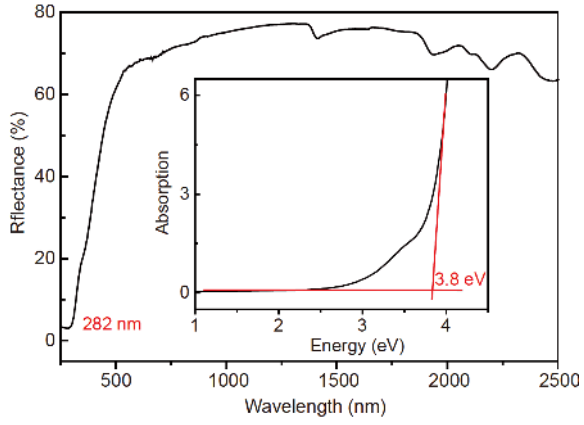

Figure 5 The UV-Vis-NIR diffuse reflectance spectra of $K_7CaBi_2B_{15}O_{30}$.

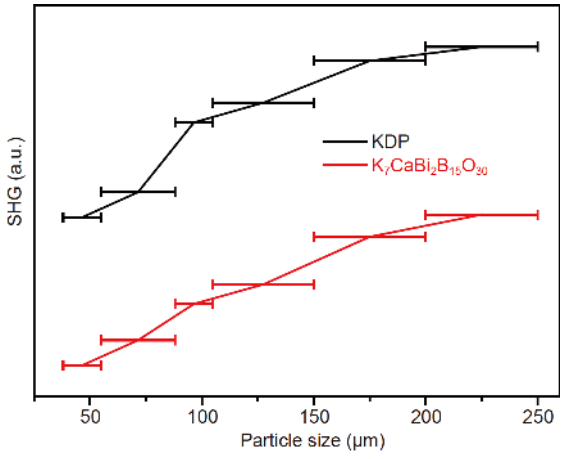

Figure 6 SHG intensity *vs.* particle size for KDP and $K_7CaBi_2B_{15}O_{30}$.

pole moments [72] for BO_3 and BO_4 were explored to better understand the contribution of each group (Table S8). The results indicate that B(1,2)O_3 (2.778 and 10.250 Debye) have larger dipole moments than B(3)O_4 (1.624 Debye) tetrahedron, which is consistent with anionic group theory. And the arrangement of the B–O groups also can determine their overall NLO contribution. It can be seen that the isolated B_5O_{10} groups are not arranged parallel in the structure (Fig. 3c), and this arrangement may have a negative impact on the SHG response. Besides, the BiO_6 octahedra also have large dipole moments (4.432 Debye), while the CaO_6 octahedra show small values. According to previous reports [73], the distortion directions of BiO_6 octahedra belong to the C_3 type (face) with the distortion value 0.281, and the CaO_6 octahedra are regular without distortion (Table S9). The above calculated results indicate that the distorted BiO_6 octahedra make some contribution to the SHG response, and the CaO_6 octahedra contribute little.

Theoretical analysis

To better understand the origins of the optical properties, the band structure, density of states and the SHG-density were calculated and the results are shown in Figs 7–9, respectively. For Compound **I**, the top of VBs is located at point Z and the bottom of CBs is at point G, which indicates that it has an indirect-band-gap characteristic and the value of the band gap is 3.54 eV (Fig. 7a), which is smaller than the experimental value (3.8 eV). For Compound **II**, the top of VBs and the bottom of CBs are at the same point G, indicating that it is a direct-band-gap characteristic and the value of the band gap is 3.95 eV (Fig. 7b).

The total and partial densities of states (TDOS and PDOS) of Compounds **I** and **II** are shown in Fig. 8a and b. For Compounds **I** and **II**, the VBs can be divided into

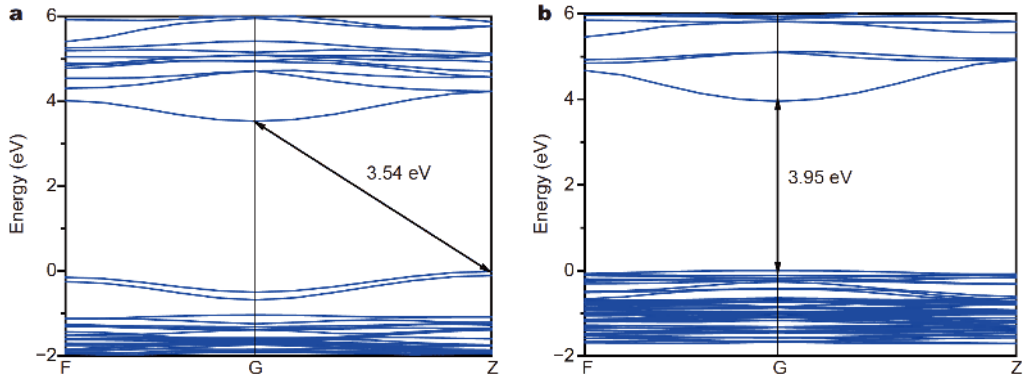

Figure 7 Calculated band structures of (a) $K_7CaBi_2B_{15}O_{30}$ and (b) $K_7CaLa_2B_{15}O_{30}$.

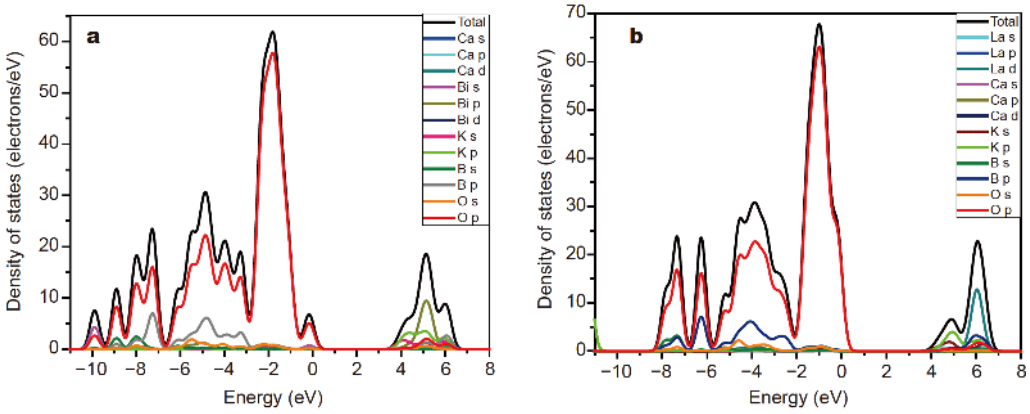

Figure 8 TDOS and PDOS of (a) $K_7CaBi_2B_{15}O_{30}$ and (b) $K_7CaLa_2B_{15}O_{30}$.

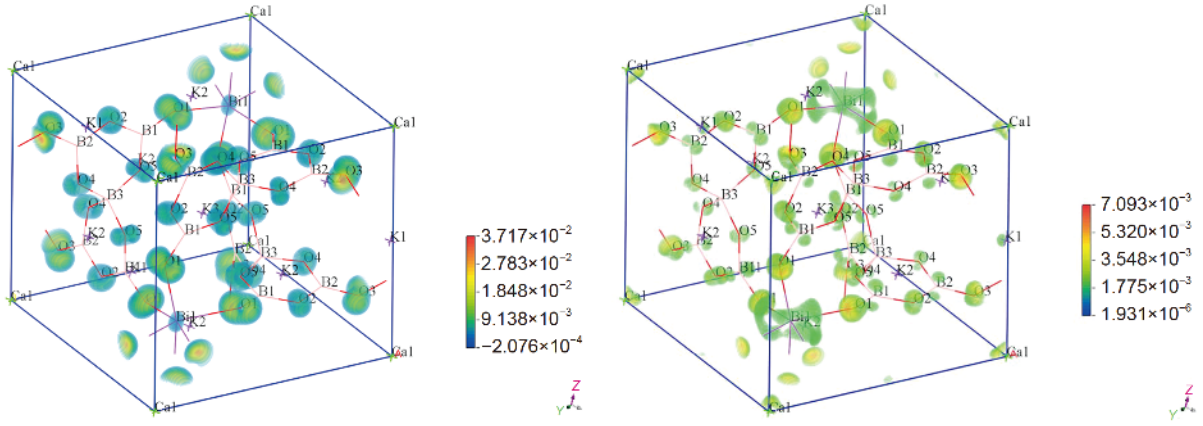

Figure 9 The SHG–density of VE occupied (a) and unoccupied states (b) of $K_7CaBi_2B_{15}O_{30}$.

three regions: firstly, the bands in the lower region (−21 to −16 eV) mainly come from Ca 3p, B 2s2p and O 2s orbitals, which originate from the interactions of Ca–O and B–O bonds. Secondly, the bands in the middle region (−13 to −10 eV) mainly come from K 3p orbitals. Thirdly, the bands in the top region (−10 to −3 eV) mainly come

from B 2s2p and O 2p orbitals. And the upper part of VB from −3 eV to Fermi level (FL) shows some of the hybridizations between B 2p and O 2p orbitals, revealing a few of chemical bonds between the B–O, but the top VB maximum is dominated by O 2p orbitals. In addition, for the bottom of CB to 7 eV, it is dominated by the orbitals of Bi 6p, La 5d, B 2p, K 3p, and O 2p, and the Bi 6p, La 5d, and B 2p orbitals determine the CB minimum of Compounds **I** and **II**, respectively.

The SHG coefficient of Compound **I** was also obtained based on DFT calculations [74]. The calculated d_{11} and d_{12} are 1.27 and −1.27 pm V^{-1}, which are about three times that of KDP d_{36}= 0.39 pm V^{-1}. The calculated d_{14} is very small and can be neglected. In addition, the SHG-density technique was applied to analyze the contribution of NLO-active units for the SHG effect. Fig. 9 shows the SHG density of the VE transition process. It clearly shows that the O atoms play an important role in the occupied states. Besides, the Bi atoms also make some contribution to SHG in the occupied states. And the Bi, B, and O atoms make a major contribution to the unoccupied states. In addition, the B atoms, which make the major contribution to the SHG response, are all connected with three O atoms to form the BO_3 groups, which is consistent with anionic group theory. The analysis results show that the π-conjugated BO_3 groups and distortion BiO_6 octahedra are important NLO-active units to enhance the SHG response.

CONCLUSIONS

Three new crystals ($K_7CaLa_2B_{15}O_{30}$, $K_7CaBi_2B_{15}O_{30}$, and $K_7BaBi_2B_{15}O_{30}$) were synthesized. Though the title compounds are stoichiometrically equivalent and share a similar bonding network, they crystallize in different space groups. A detailed structural analysis reveals that the difference between the cation sizes of Ca^{2+} and K^+/Ba^{2+} is the major factor for the different framework structure. The UV cut-off edge estimated from the UV-Vis-NIR spectrum for $K_7CaBi_2B_{15}O_{30}$ is about 282 nm. In addition, $K_7CaBi_2B_{15}O_{30}$ shows moderate powder SHG intensities about 0.6 times that of KDP with phase-matching behavior at 1,064 nm. Furthermore, the dipole moments and the DFT calculations indicate that the SHG response mainly comes from the BO_3 groups and distorted BiO_6 octahedra. Considering the short UV cut-off edge and a moderate SHG response, $K_7CaBi_2B_{15}O_{30}$ may have potential applications in the UV range as NLO materials.

Received 5 February 2019; accepted 9 March 2019; published online 22 March 2019

1 Chen CT, Sasaki T, Li RK, *et al*. Nonlinear Optical Borate Crystals: Principals and Applications. Weinheim: John Wiley & Sons, 2012
2 Feng JH, Hu CL, Xia HP, *et al*. $Li_7(TeO_3)_3F$: a lithium fluoride tellurite with large second harmonic generation responses and a short ultraviolet cutoff edge. Inorg Chem, 2017, 56: 14697–14705
3 Wu H, Pan S, Poeppelmeier KR, *et al*. $K_3B_6O_{10}Cl$: a new structure analogous to perovskite with a large second harmonic generation response and deep UV absorption edge. J Am Chem Soc, 2011, 133: 7786–7790
4 Feng J, Xu X, Hu CL, *et al*. $K_6ACaSc_2(B_5O_{10})_3$ (A = Li, Na, $Li_{0.7}Na_{0.3}$): nonlinear-optical materials with short UV cutoff edges. Inorg Chem, 2019, 58: 2833–2839
5 Zou G, Lin C, Jo H, *et al*. Pb_2BO_3Cl: a tailor-made polar lead borate chloride with very strong second harmonic generation. Angew Chem Int Ed, 2016, 55: 12078–12082
6 Pan Y, Guo SP, Liu BW, *et al*. Second-order nonlinear optical crystals with mixed anions. Coord Chem Rev, 2018, 374: 464–496
7 Zhang J, Shah SAA, Hao Y, *et al*. Weak fatigue notch sensitivity in a biomedical titanium alloy exhibiting nonlinear elasticity. Sci China Mater, 2018, 61: 537–544
8 Chen CT, Wu BC, Jiang AD, You GM. A new-type ultraviolet SHG crystal β-BaB_2O_4. Sci Sin Ser B, 1985, 589: 235–243
9 Chen C, Wu Y, Jiang A, *et al*. New nonlinear-optical crystal: LiB_3O_5. J Opt Soc Am B, 1989, 6: 616–621
10 Wu Y, Sasaki T, Nakai S, *et al*. CsB_3O_5: a new nonlinear optical crystal. Appl Phys Lett, 1993, 62: 2614–2615
11 Tu JM, Keszler DA. $CsLiB_6O_{10}$: a noncentrosymmetric polyborate. Mater Res Bull, 1995, 30: 209–215
12 Chen C, Xu Z, Deng D, *et al*. The vacuum ultraviolet phase-matching characteristics of nonlinear optical $KBe_2BO_3F_2$ crystal. Appl Phys Lett, 1996, 68: 2930–2932
13 Chen C, Wang Y, Wu B, *et al*. Design and synthesis of an ultraviolet-transparent nonlinear optical crystal $Sr_2Be_2B_2O_7$. Nature, 1995, 373: 322–324
14 Ye N, Zeng W, Jiang J, *et al*. New nonlinear optical crystal $K_2Al_2B_2O_7$. J Opt Soc Am B, 2000, 17: 764–768
15 Bierlein JD, Arweiler CB. Electro-optic and dielectric properties of $KTiOPO_4$. Appl Phys Lett, 1986, 49: 917–919
16 Slater JC. Theory of the transition in KH_2PO_4. J Chem Phys, 1941, 9: 16–33
17 Boyd G, Kasper H, McFee J. Linear and nonlinear optical properties of $AgGaS_2$, $CuGaS_2$, and $CuInS_2$, and theory of the wedge technique for the measurement of nonlinear coefficients. IEEE J Quantum Electron, 1971, 7: 563–573
18 Kildal H, Mikkelsen JC. The nonlinear optical coefficient, phase-matching, and optical damage in the chalcopyrite $AgGaSe_2$. Optics Commun, 1973, 9: 315–318
19 Boyd GD, Buehler E, Storz FG. Linear and nonlinear optical properties of $ZnGeP_2$ and CdSe. Appl Phys Lett, 1971, 18: 301–304
20 Dong X, Shi Y, Zhou Z, *et al*. $M_2Cd_3B_{16}O_{28}$ (M = Rb, Cs): two isostructural alkali cadmium borates with a new type of borate layer. Eur J Inorg Chem, 2013, 2013(2): 203–207
21 Jiang D, Wang Y, Zhang B, *et al*. $K_{11}RbB_{28}O_{48}$: a new triple-layered borate with an unprecedented $[B_{28}O_{57}]$ fundamental building block. Dalton Trans, 2018, 47: 10833–10836
22 Wu H, Yu H, Pan S, *et al*. New type of complex alkali and alkaline earth metal borates with isolated $(B_{12}O_{24})^{12-}$ anionic group. Dalton Trans, 2014, 43: 4886
23 Wei Q, Wang JJ, He C, *et al*. Deep-ultraviolet nonlinear optics in a

borate framework with 21-ring channels. Chem Eur J, 2016, 22: 10759–10762
24 Zhang X, Wu H, Yu H, *et al.* $Ba_4M(CO_3)_2(BO_3)_2$ (M=Ba, Sr): two borate-carbonates synthesized by open high temperature solution method. Sci China Mater, 2019, 62
25 Xia Z, Poeppelmeier KR. Chemistry-inspired adaptable framework structures. Acc Chem Res, 2017, 50: 1222–1230
26 Dong X, Jing Q, Shi Y, *et al.* $Pb_2Ba_3(BO_3)_3Cl$: a material with large SHG enhancement activated by Pb-chelated BO_3 groups. J Am Chem Soc, 2015, 137: 9417–9422
27 Mutailipu M, Zhang M, Wu H, *et al.* $Ba_3Mg_3(BO_3)_3F_3$ polymorphs with reversible phase transition and high performances as ultraviolet nonlinear optical materials. Nat Commun, 2018, 9: 3089–3090
28 Liu L, Su X, Yang Y, *et al.* $Ba_2B_{10}O_{17}$: a new centrosymmetric alkaline-earth metal borate with a deep-UV cut-off edge. Dalton Trans, 2014, 43: 8905–8910
29 Shan F, Kang L, Zhang G, *et al.* $Na_3Y_3(BO_3)_4$: a new non-centrosymmetric borate with an open-framework structure. Dalton Trans, 2016, 45: 7205–7208
30 Wu C, Yang G, Humphrey MG, *et al.* Recent advances in ultraviolet and deep-ultraviolet second-order nonlinear optical crystals. Coord Chem Rev, 2018, 375: 459–488
31 Luo M, Ye N, Zou G, *et al.* $Na_8Lu_2(CO_3)_6F_2$ and $Na_3Lu(CO_3)_2F_2$: rare earth fluoride carbonates as deep-UV nonlinear optical materials. Chem Mater, 2013, 25: 3147–3153
32 Tran TT, He J, Rondinelli JM, *et al.* $RbMgCO_3F$: a new beryllium-free deep-ultraviolet nonlinear optical material. J Am Chem Soc, 2015, 137: 10504–10507
33 Zhao S, Gong P, Bai L, *et al.* Beryllium-free $Li_4Sr(BO_3)_2$ for deep-ultraviolet nonlinear optical applications. Nat Commun, 2014, 5: 4019–4026
34 Zou G, Lin C, Kim H, *et al.* $Rb_2Na(NO_3)_3$: a congruently melting UV-NLO crystal with a very strong second-harmonic generation response. Crystals, 2016, 6: 42
35 Zhang W, Halasyamani PS. Crystal growth and optical properties of a UV nonlinear optical material $KSrCO_3F$. CrystEngComm, 2017, 19: 4742–4748
36 Zou G, Jo H, Lim SJ, *et al.* $Rb_3VO(O_2)_2CO_3$: a four-in-one carbonatoperoxovanadate exhibiting an extremely strong second-harmonic generation response. Angew Chem Int Ed, 2018, 57: 8619–8622
37 Dong X, Huang L, Liu Q, *et al.* Perfect balance harmony in $Ba_2NO_3(OH)_3$: a beryllium-free nitrate as a UV nonlinear optical material. Chem Commun, 2018, 54: 5792–5795
38 Zou G, Lin Z, Zeng H, *et al.* $Cs_3VO(O_2)_2CO_3$: an exceptionally thermostable carbonatoperoxovanadate with an extremely large second-harmonic generation response. Chem Sci, 2018, 9: 8957–8961
39 Han G, Liu Q, Wang Y, *et al.* Experimental and theoretical studies on the linear and nonlinear optical properties of lead phosphate crystals $LiPbPO_4$. Phys Chem Chem Phys, 2016, 18: 19123–19129
40 Liu L, Zhang B, Zhang F, *et al.* $Pb_6Ba_2(BO_3)_5X$ (X = Cl, Br): new borate halides with strong predicted optical anisotropies derived from Pb^{2+} and $(BO_3)^{3-}$. Dalton Trans, 2015, 44: 7041–7047
41 Mao FF, Hu CL, Xu X, *et al.* $Bi(IO_3)F_2$: the first metal iodate fluoride with a very strong second harmonic generation effect. Angew Chem, 2017, 129: 2183–2187
42 Liang ML, Hu CL, Kong F, *et al.* $BiFSeO_3$: an excellent SHG material designed by aliovalent substitution. J Am Chem Soc, 2016, 138: 9433–9436
43 Dong X, Huang L, Hu C, *et al.* $CsSbF_2SO_4$: an excellent ultraviolet nonlinear optical sulfate with a $KTiOPO_4$ (KTP)-type structure. Angew Chem, 2019
44 Yamada M, Nada N, Saitoh M, *et al.* First-order quasi-phase matched $LiNbO_3$ waveguide periodically poled by applying an external field for efficient blue second-harmonic generation. Appl Phys Lett, 1993, 62: 435–436
45 Yu H, Wu H, Pan S, *et al.* $Cs_3Zn_6B_9O_{21}$: a chemically benign member of the KBBF family exhibiting the largest second harmonic generation response. J Am Chem Soc, 2014, 136: 1264–1267
46 Jo H, Ok KM. Polar noncentrosymmetric $ZnMoSb_2O_7$ and nonpolar centrosymmetric $CdMoSb_4O_{10}$: d^{10} transition metal size effect influencing the stoichiometry and the centricity. Inorg Chem, 2016, 55: 6286–6293
47 Mutailipu M, Xie Z, Su X, *et al.* Chemical cosubstitution-oriented design of rare-earth borates as potential ultraviolet nonlinear optical materials. J Am Chem Soc, 2017, 139: 18397–18405
48 Xie Z, Mutailipu M, He G, *et al.* A series of rare-earth borates $K_7MRE_2B_{15}O_{30}$ (M = Zn, Cd, Pb; RE = Sc, Y, Gd, Lu) with large second harmonic generation responses. Chem Mater, 2018, 30: 2414–2423
49 Zhang J, Kang L, Lin TH, *et al.* The mechanism for the nonlinear optical properties in $La_9Na_3B_8O_{27}$, $La_2Na_3B_3O_9$ and $La_2CaB_{10}O_{19}$: *ab initio* studies. J Phys-Condens Matter, 2015, 27: 485501
50 Aka G, Kahn-Harari A, Mougel F, *et al.* Linear- and nonlinear-optical properties of a new gadolinium calcium oxoborate crystal, $Ca_4GdO(BO_3)_3$. J Opt Soc Am B, 1997, 14: 2238–2247
51 He R, Lin ZS, Lee MH, *et al. Ab initio* studies on the mechanism for linear and nonlinear optical effects in $YAl_3(BO_3)_4$. J Appl Phys, 2011, 109: 103510
52 Iwai M, Kobayashi T, Furuya H, *et al.* Crystal growth and optical characterization of rare-earth (Re) calcium oxyborate $ReCa_4O(BO_3)_3$ (Re = Y or Gd) as new nonlinear optical material. Jpn J Appl Phys, 1997, 36: L276–L279
53 SAINT, Version 7.60A. Bruker Analytical X-ray Instruments, Inc.: Madison, WI, 2008
54 Sheldrick GM. Crystal structure refinement with SHELXL. Acta Crystlogr C Struct Chem, 2015, 71: 3–8
55 Dolomanov OV, Bourhis LJ, Gildea RJ, *et al.* OLEX2: a complete structure solution, refinement and analysis program. J Appl Crystlogr, 2009, 42: 339–341
56 Li J, Wang K, Song S, *et al.* $[LiNa(N_5)_2(H_2O)_4]\cdot H_2O$: a novel heterometallic cyclo-N_5^- framework with helical chains. Sci China Mater, 2018, 62: 283–288
57 Spek AL. Single-crystal structure validation with the program PLATON. J Appl Crystlogr, 2003, 36: 7–13
58 Kurtz SK, Perry TT. A powder technique for the evaluation of nonlinear optical materials. J Appl Phys, 1968, 39: 3798–3813
59 Segall MD, Lindan PJD, Probert MJ, *et al.* First-principles simulation: ideas, illustrations and the castep code. J Phys-Condens Matter, 2002, 14: 2717–2744
60 Li X, Hui Q, Shao D, *et al.* First-principles study on the stability and electronic structure of Mg/ZrB_2 interfaces. Sci China Mater, 2016, 59: 28–37
61 Chen ZQ, Hu M, Li CM, *et al.* Electronic structures, elastic and optical properties of M_2O_5 (M = V, Nb, Ta). Sci China Mater, 2016, 59: 265–278
62 Fonseca Guerra C, Snijders JG, te Velde G, *et al.* Towards an order-N DFT method. Theor Chem Accounts-Theor Computation

Modeling (Theoretica Chim Acta), 1998, 99: 391–403
63 Wu B, Yin J, Ding Y, *et al.* A new two-dimensional $TeSe_2$ semiconductor: indirect to direct band-gap transitions. Sci China Mater, 2017, 60: 747–754
64 Meng R, Jiang J, Liang Q, *et al.* Design of graphene-like gallium nitride and WS_2/WSe_2 nanocomposites for photocatalyst applications. Sci China Mater, 2016, 59: 1027–1036
65 Zhang B, Lee MH, Yang Z, *et al.* Simulated pressure-induced blue-shift of phase-matching region and nonlinear optical mechanism for $K_3B_6O_{10}X$ (X = Cl, Br). Appl Phys Lett, 2015, 106: 031906
66 Lin J, Lee MH, Liu ZP, *et al.* Mechanism for linear and nonlinear optical effects in β-BaB_2O_4 crystals. Phys Rev B, 1999, 60: 13380–13389
67 Brown ID, Altermatt D. Bond-valence parameters obtained from a systematic analysis of the inorganic crystal structure database. Acta Crystlogr B Struct Sci, 1985, 41: 244–247
68 Zhao S, Zhang G, Yao J, *et al.* $K_6Li_3Sc_2B_{15}O_{30}$: a new nonlinear optical crystal with a short absorption edge. CrystEngComm, 2012, 14: 5209–5214
69 Tran TT, Koocher NZ, Rondinelli JM, *et al.* Beryllium-free β-$Rb_2Al_2B_2O_7$ as a possible deep-ultraviolet nonlinear optical material replacement for $KBe_2BO_3F_2$. Angew Chem Int Ed, 2017, 56: 2969–2973
70 Yang Y, Pan S, Hou X, *et al.* A congruently melting and deep UV nonlinear optical material: $Li_3Cs_2B_5O_{10}$. J Mater Chem, 2011, 21: 2890
71 Chen C, Wu Y, Li R. The anionic group theory of the non-linear optical effect and its applications in the development of new high-quality NLO crystals in the borate series. Int Rev Phys Chem, 1989, 8: 65–91
72 Maggard PA, Nault TS, Stern CL, *et al.* Alignment of acentric $MoO_3F_3^{3-}$ anions in a polar material: $(Ag_3MoO_3F_3)(Ag_3MoO_4)Cl$. J Solid State Chem, 2003, 175: 27–33
73 Halasyamani PS. Asymmetric cation coordination in oxide materials: influence of lone-pair cations on the intra-octahedral distortion in d^0 transition metals. Chem Mater, 2004, 16: 3586–3592
74 Rashkeev SN, Lambrecht WRL, Segall B. Efficient *ab-initio* method for the calculation of frequency dependent non-linear optical response in semiconductors: application to second harmonic generation. Physics, 1997, 46: 3848–3859

Acknowledgements This work is supported by the West Light Foundation of the CAS (2016-YJRC-2 and 2015 XBQN-B-11), the National Natural Science Foundation of China (51602341 and 91622107), the Natural Science Foundation of Xinjiang (2016D01B061), Tianshan Innovation Team Program (2018D14001), and Key research project of Frontier Science of CAS (QYZDB-SSW-JSC049).

Author contributions Xie Z, Wang Y and Han G performed the experiments, data analysis, and wrote the paper; Cheng S and Yang Z performed the theoretical data analysis; Pan S designed and supervised the experiments. All authors contributed to the general discussion.

Conflict of interest The authors declare that they have no conflict of interest.

Supplementary information The supporting data are available in the online version of the paper.

Zhiqing Xie received his BSc degree in Nanshan College in 2015. Now, he joined Professor Shilie Pan's research group as a master student at Xinjiang University. He is currently focusing on the optical materials.

Ying Wang received his BSc degree in applied chemistry from Peking University in 2009. Under the supervision of Professor Shilie Pan at the University of Chinese Academy of Sciences (UCAS), he completed his PhD in material physics and chemistry in 2015. In the same year, he started his independent career as an assistant professor at Xinjiang Technical Institute of Physics & Chemistry of CAS (XTIPC, CAS). In 2017, he was promoted to associate professor at XTIPC. His current research interests center on optical materials.

Shilie Pan received his BSc degree in chemistry from Zhengzhou University in 1996. He completed his PhD under the supervision of Professor Yicheng Wu (Academician) at the University of Science & Technology of China in 2002. From 2002 to 2004, he was a post-doctoral fellow at the Technical Institute of Physics & Chemistry of CAS in the laboratory of Professor Chuangtian Chen (Academician). From 2004 to 2007, he was a post-doctoral fellow at Northwestern University in the laboratory of Professor Kenneth R. Poeppelmeier in USA. From 2007, he worked as a full professor at XTIPC of CAS. His current research interests include the design, synthesis, crystal growth, and evaluation of new optical-electronic functional materials.

新的非线性光学材料$K_7MRE_2B_{15}O_{30}$ (M= Ca and Ba, RE= La and Bi)的合成、表征和理论分析

解植擎[1†], 王颖[1†], 程世超[1], 韩国鹏[1,2], 杨志华[1], 潘世烈[1*]

摘要 本文采用高温熔液法合成了三种新型复合硼酸盐化合物$K_7CaBi_2B_{15}O_{30}$、$K_7CaLa_2B_{15}O_{30}$和$K_7BaBi_2B_{15}O_{30}$. $K_7CaLa_2B_{15}O_{30}$和$K_7CaBi_2B_{15}O_{30}$结晶于三方手性空间群*R*32中, $K_7BaBi_2B_{15}O_{30}$结晶于非中心对称正交极性空间群$Pca2_1$. 这三个化合物具有相似的三维晶体结构, 由孤立的B_5O_{10}基团和LaO_6或BiO_6八面体组成, K^+、Ca^{2+}、Ba^{2+}阳离子填充于空隙中以保持电荷平衡. 根据我们的调研, 在$K_7M^{II}RE_2B_{15}O_{30}$体系内($M^{II}$ = Ca, Sr, Ba, Zn, Cd, Pb, K/$RE_{0.5}$; RE = Sc, Y, La, Gd, Lu, Bi), $K_7BaBi_2B_{15}O_{30}$是唯一一个结晶于不同空间群的化合物, 其丰富了硼酸盐的结构化学. 详细的结构分析表明, 碱土金属阳离子的尺寸和配位数的差异是导致结构变化的主要原因. 此外, UV-Vis-NIR光谱分析和倍频效应(SHG)测试表明$K_7CaBi_2B_{15}O_{30}$具有较短的截止边(大约282 nm)和适中的倍频效应(约0.6×KDP). 我们还进行了热重差热和红外光谱的测试. 为了更好地理解上述化合物的结构性能关系, 我们还进行了第一性原理计算.

